Applied Thermal Engineering 303 (2026) 132522

Contents lists available at ScienceDirect

Applied Thermal Engineering

journal homepage: www.elsevier.com/locate/apthermeng

Research Paper

Experimental and modelling investigation of thermohydraulic performance of CO_2 finned-tube condensers

Lei Chai [*], Savvas A. Tassou

Centre for Sustainable Energy Use in Food Chains (CSEF), Department of Mechanical and Aerospace Engineering, Brunel University of London, Uxbridge, Middlesex UB8 3PH, UK

ARTICLE INFO

Keywords:
Thermohydraulic performance
CO_2 finned-tube condenser
Experimental analysis
Model development

ABSTRACT

Carbon dioxide is a promising refrigerant for refrigeration and heat pump applications because of its environmental sustainability. However, unlike supercritical gas coolers, the thermohydraulic behaviour of subcritical CO_2 finned-tube condensers remains inadequately investigated and understood because of complex condensation and two-phase flow phenomena. This study presents a combined experimental and numerical investigation of a CO_2 finned-tube condenser operating under subcritical conditions. Experiments were conducted using a dedicated CO_2 test facility equipped with a two-row finned-tube heat exchanger and comprehensive instrumentation for measuring refrigerant- and air-side operating parameters. A distributed segment-by-segment effectiveness–NTU model was developed and validated to predict local and overall thermohydraulic performance. The model captures the coupled heat transfer, phase-change, and pressure-drop processes occurring in both the superheated and two-phase regions of the condenser. Validation against 30 operating conditions demonstrated deviations within ±10% for heat transfer rate, ±15% for refrigerant-side pressure drop, and ±10% for air-side pressure drop. The effects of refrigerant mass flow rate, air velocity, and inlet air temperature on local and average heat transfer and pressure-drop characteristics were systematically examined. The results provide new insight into the evolution of condensation, vapour quality, and local heat transfer coefficients along the flow path, and offer a reliable tool for the design and optimisation of high-efficiency CO_2 refrigeration and heat pump systems.

1. Introduction

The increasing global demand for energy-efficient and environmentally sustainable refrigeration and heat pump technologies has intensified interest in natural refrigerants, owing to their negligible ozone depletion potential and low global warming potential [1]. Among these, carbon dioxide (CO_2, R744) has emerged as a promising working fluid for trans-critical and subcritical refrigeration cycles, heat pump systems, automotive air conditioning, and industrial thermal applications. This is primarily attributed to its favourable thermophysical properties, including high volumetric cooling capacity, elevated thermal conductivity, and enhanced heat transfer characteristics in the vicinity of the pseudo-critical region [2]. Nevertheless, the practical implementation of CO_2 systems introduces significant challenges, particularly in the design and optimisation of heat exchangers such as gas coolers and condensers, where a delicate balance between heat transfer enhancement and pressure drop minimization is essential for achieving high system efficiency. Throughout this paper, the term gas cooler refers to heat rejection from supercritical CO_2 without phase change, whereas condenser refers to heat rejection under subcritical conditions involving vapour-to-liquid phase transition.

Aluminium microchannel heat exchangers and finned-tube heat exchangers represent two of the most widely employed heat exchanger configurations in CO_2-based systems [3,4]. Microchannel heat exchangers utilize flat multiport aluminium tubes with small hydraulic diameters, which enables high heat transfer coefficients, reduced refrigerant charge, and compact system design [5]. However, these systems are susceptible to flow maldistribution, fouling, and limited serviceability. In contrast, finned-tube heat exchangers consist of circular tubes with extended surfaces to enhance air-side heat transfer. These systems offer superior mechanical robustness, improved tolerance to high trans-critical pressures, and greater resilience to flow non-uniformities [6]. Despite their larger size and higher refrigerant inventory, finned-tube configurations are widely adopted in industrial and air-cooled applications due to their durability and ease of maintenance.

* Corresponding author.
E-mail address: Lei.Chai@brunel.ac.uk (L. Chai).

https://doi.org/10.1016/j.applthermaleng.2026.132522
Received 17 April 2026; Received in revised form 20 July 2026; Accepted 22 July 2026
Available online 23 July 2026

Nomenclature

C	Correlation parameter
CFD	Computational fluid dynamics
C_{min}	Minimum heat capacity rate, W/K
D	Diameter, m
D_c	Fin collar outside diameter, m
f	Friction factor
f_1-f_7	Correlation parameters
g	Acceleration due to gravity, m/s^2
h	Heat transfer coefficient, W/(m^2·K)
h_{air}	Specific enthalpy of air, J/kg
h_{CO_2}	Specific enthalpy of CO_2, J/kg
h_I	Heat transfer coefficient given by Eq. (A.2), W/(m^2·K)
h_{LO}	Heat transfer coefficient assuming liquid phase flowing alone in the tube, W/(m^2·K)
h_{Nu}	Heat transfer coefficient given by Eq. (A.3), W/(m^2·K)
i	Segment number
j	Colburn factor
j_1-j_7	Correlation parameters
J_g	Correlation parameter
k	Thermal conductivity, W/(m·K)
L	Length, m
$L_{CO_2,\ x}$	Local tube length measured along CO_2 flow direction, m
$\dot{m}$	Mass flow rate, kg/s
NTU	Number of transfer unit
N	Number of tube rows
Nu	Nusselt number
P	Pressure, Pa
P_l	Longitudinal tube pitch, m
Pr	Prandtl number
P_t	Transverse tube pitch, m
$\dot{Q}$	Heat transfer rate, W
Re	Reynolds number
Re_{Dc}	Reynolds number based on tube collar diameter
S_h	Slit height, m
S_n	Slit number in an enhanced zone
S_s	Slit breadth in the airflow direction, m
T	Temperature, K
v	Velocity, m/s
x	Mass quality
X	Lockhart-Martinelli parameter
Z	Correlation parameter
ΔP	Pressure drop, Pa
Greek letters	
ρ	Density, kg/m^3
μ	Dynamic viscosity, Pa·s
ε	Heat exchanger effectiveness
ϕ_L^2	Lockhart-Martinelli two-phase multiplier
Subscripts	
air	Cooling air
exp	Experiment
G	Vapour phase
i	Segment number
in	Inlet
L	Liquid phase
LO	Liquid phase flowing alone in the tube
min	Minimum
out	Outlet
TP	Two-phase

In such systems, the dominant thermal resistance typically lies on the air side, which makes fin design and airflow distribution critical to overall performance [7,8]. Despite the increasing deployment of CO_2 systems, accurate prediction of heat transfer and pressure drop in finned-tube heat exchangers remains challenging [9]. This is largely due to the strong variation of CO_2 thermophysical properties near the pseudo-critical region. These variations significantly influence convective heat transfer and pressure drop, limiting the applicability of conventional correlations developed for traditional refrigerants. Furthermore, air-side parameters, including velocity, temperature, and fin geometry, strongly affect overall thermal and hydraulic performance, which necessitates detailed investigation of their combined effects.

Experimental investigations have been extensively conducted to characterise the thermohydraulic performance of CO_2 finned-tube heat exchangers operating under supercritical conditions. Tsamos et al. [10] systematically evaluated the influence of gas cooler/condenser design on the performance of a CO_2 booster refrigeration system and demonstrated that heat exchanger effectiveness plays a critical role in determining optimal discharge pressure and system coefficient of performance. Their results indicated that even minor variations in gas cooler configuration can lead to significant changes in seasonal energy consumption. Santosa et al. [11] provided detailed measurements of air-side and refrigerant-side heat transfer coefficients and showed significant spatial non-uniformity along the heat exchanger and strong sensitivity to operating conditions, particularly near the pseudo-critical region. Their findings highlighted the limitations of conventional uniform heat transfer assumptions and emphasised the combined influence of air- and refrigerant-side thermal resistances on overall performance. Vojáček et al. [12] experimentally evaluated an air-cooled finned-tube supercritical CO_2 heat exchanger and demonstrated that thermohydraulic performance is strongly dependent on inlet air conditions and operating pressure, especially in regions of rapid property variation. Furthermore, Zhang and Ge [13] investigated the effect of fin heat conduction, showing that axial and transverse conduction significantly reduces fin efficiency under high thermal gradients, thereby affecting local temperature distribution and overall heat transfer predictions.

Numerical simulation has also been extensively employed to investigate the thermohydraulic performance of CO_2 finned-tube heat exchangers, providing detailed insight into heat transfer, pressure drop, and flow distribution mechanisms that are difficult to resolve experimentally. Ge and Cropper [14] developed a simulation framework for finned-tube CO_2 gas coolers, which incorporated the strong thermophysical property variations near the pseudo-critical region and demonstrated high sensitivity of performance to discharge pressure, ambient temperature, and airflow conditions. Chai et al. [9] proposed an improved thermohydraulic model with enhanced prediction capability, validated against experimental data across a wide range of operating conditions, and highlighted the influence of operating pressure, inlet air temperature, and mass flow rate. Alexopoulos et al. [15] analysed the design and performance of finned-tube CO_2 gas coolers for residential applications and demonstrated the significant impact of geometric and operating parameters on system efficiency and optimal discharge pressure. Advanced computational fluid dynamics (CFD) studies have further explored spatial non-uniformities and flow distribution effects. Zhang et al. [16] showed that air maldistribution leads to reduced heat transfer effectiveness due to local deterioration of heat transfer coefficients and increased temperature non-uniformity. To address these limitations, Zhang et al. [17] developed a coupled 1D—3D CFD modelling framework, which integrated detailed air-side flow with refrigerant-side heat transfer to capture complex interactions between airflow distribution, heat transfer, and pressure drop, and achieved improved predictive accuracy compared to conventional approaches.

Additional numerical investigations have emphasised the role of buoyancy and non-uniform flow conditions. Zhou et al. [18] demonstrated that gravity effects and inlet maldistribution significantly influence local heat transfer behaviour, particularly near the pseudo-critical region, resulting in pronounced spatial variations. Moreover, system-level simulations incorporating enhanced cooling strategies have been explored. Lata and Gupta [19] showed that evaporative cooling of finned-tube gas coolers significantly improves performance under high ambient temperatures by reducing approach temperature and optimal discharge pressure. Chai et al. [20] demonstrated that spray-cooled gas coolers can substantially enhance heat rejection and lead to improved system performance.

Despite substantial advances in the experimental and numerical investigation of CO_2 finned-tube heat exchangers, research has predominantly focused on supercritical gas coolers, in which CO_2 remains in a single-phase state throughout the heat rejection process. Consequently, the thermohydraulic behaviour of subcritical CO_2 finned-tube condensers remains insufficiently understood, particularly with respect to the coupled evolution of refrigerant phase distribution, local heat transfer characteristics, and pressure losses along the flow path [21]. Most published investigations of CO_2 condensers have primarily reported overall heat transfer rates or system-level performance indicators, providing limited insight into the underlying local condensation mechanisms that govern condenser effectiveness and hydraulic resistance. From a modelling perspective, the prediction of subcritical CO_2 condensation remains considerably more challenging than that of supercritical cooling because of the coexistence of single-phase and two-phase flow regions, strong variations in thermophysical properties, and the complex interactions between latent heat transfer and flow resistance. Furthermore, modelling approaches developed for supercritical gas coolers cannot be directly applied to condenser operation because they do not account for phase-change dynamics and the associated evolution of vapour quality. Although CFD methods can provide detailed flow information, their application to condensation processes is computationally expensive and remains challenging because of the complexity of interfacial transport phenomena, phase distribution, and flow-regime transitions [22]. To address these knowledge gaps, this study presents a combined experimental and modelling investigation of the thermohydraulic performance of a CO_2 finned-tube condenser operating under subcritical conditions. The novelty of this work lies in the integration of high-fidelity experimental measurements with a distributed segment-by-segment effectiveness–NTU model capable of simultaneously predicting local and overall heat transfer, vapour quality evolution, and pressure drop throughout the condenser. The model is validated against extensive experimental data covering a wide range of refrigerant and air-side operating conditions and provides detailed information on local temperature distributions, heat transfer coefficients, condensation progression, and hydraulic losses. The resulting

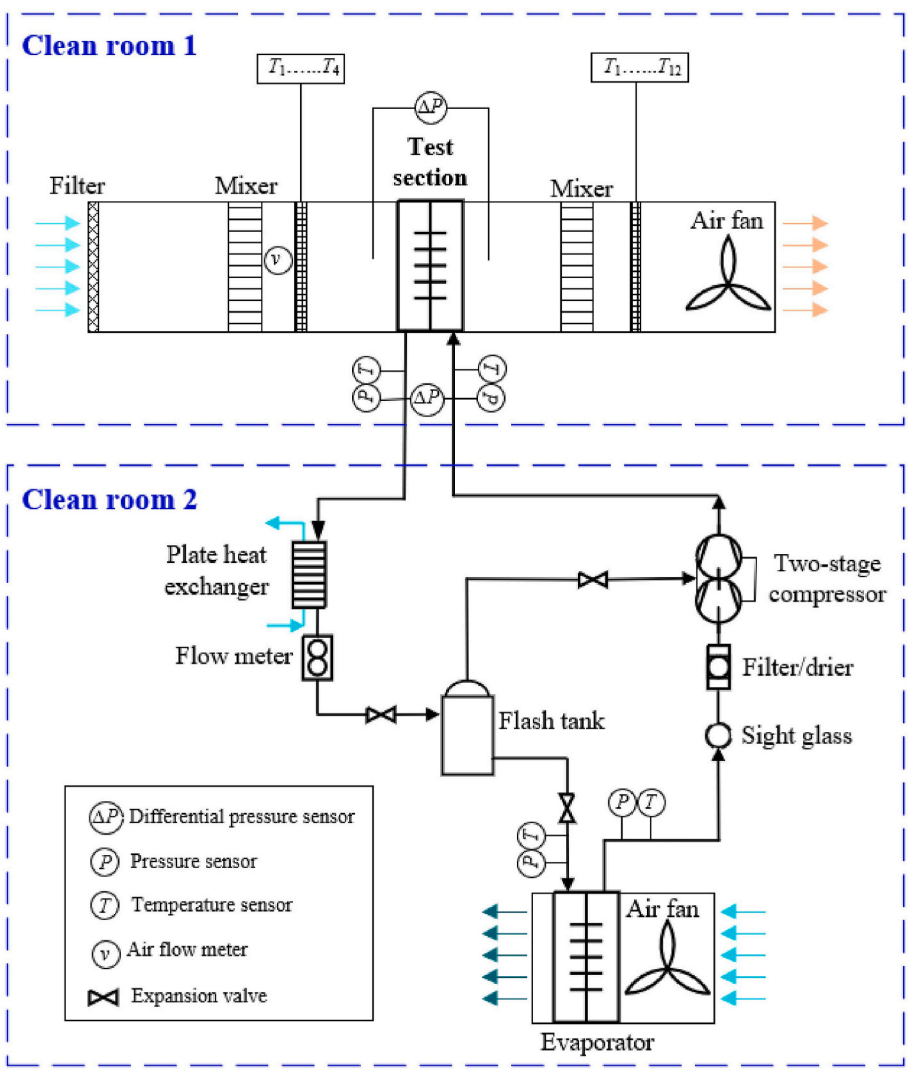

Fig. 1. Test facility and experimental instrumentation.

framework offers both improved physical understanding of subcritical CO_2 condensation and a practical design tool for the optimisation of high-efficiency CO_2 refrigeration and heat pump systems.

2. Experimental setup

2.1. Test facility

The experimental investigation was conducted using a dedicated CO_2 finned-tube heat exchanger test facility designed to evaluate heat transfer and pressure drop characteristics under well-controlled operating conditions. A schematic of the test facility and instrumentation is presented in Fig. 1. The facility consists of a closed-loop CO_2 refrigeration system. High-purity CO_2 (99.99%) is circulated using a variable-speed rotary compressor (Panasonic, Model C-CV303HOT). The compressor is a hermetic two-stage rolling piston type, capable of operating up to 125 °C and 140 bar at the discharge. The compressed CO_2 enters the tested finned-tube heat exchanger, where heat is rejected to an external air stream. A water-cooled plate heat exchanger is installed downstream of the finned-tube condenser to further reduce the CO_2 temperature before entering the expansion valve. The refrigerant is subsequently expanded through an electronic expansion valve (Carel, Model E2V14CW) to an intermediate pressure and directed into a flash tank (OCSCOLD, Model ACSRV1680570B), where phase separation occurs. Vapour is partially recirculated to the compressor through supplementary suction ports, while the liquid phase undergoes further expansion before entering a finned-tube evaporator. The evaporator consists of multi-row copper tubes with aluminium fins and operates under controlled ambient air conditions. The refrigerant is heated in the evaporator and returns to the compressor, completing the cycle.

The air-side loop of the test facility is designed to provide well-controlled and uniform airflow conditions. Ambient air is first conditioned to the desired temperature and relative humidity using an air handling unit (SmartAir, Model 9-KR SW50 N), ensuring stable and repeatable inlet conditions for the experiments. The conditioned air then passes through a high-efficiency filter, which removes particulate impurities and minimizes flow disturbances. Subsequently, the air stream flows through a honeycomb flow straightener, which reduces large-scale turbulence and redistributes the velocity profile to achieve a more uniform flow field across the test section. After flow conditioning, the air inlet temperature is measured using a thermocouple mesh grid, which provides spatially averaged and representative measurements of the airflow entering the heat exchanger. The air then passes through the finned-tube heat exchanger, where it absorbs heat from the high-temperature CO_2 refrigerant flowing inside the tubes. This process increases the air temperature while maintaining controlled flow conditions. Downstream of the heat exchanger, the air flows through a second honeycomb plate assembly, which serves to re-establish flow uniformity and minimize temperature stratification before outlet measurements are taken. The outlet air temperature is measured using a second thermocouple mesh. Finally, the air is discharged from the wind tunnel by a pull-out fan, which maintains a stable airflow rate throughout the system. The pull-out fan is an inline duct fan (Ruck Etaline EL 355 E2 01) with variable frequency drives, enabling air velocities in the range of 2.0–5.0 m/s within the wind tunnel. The overall wind tunnel configuration, including flow conditioning and measurement sections, is designed in accordance with ASHRAE Standard 41.2 [23] to ensure high measurement accuracy and repeatability. A 50 mm thick flexible elastomeric thermal insulation sheet was installed on the outside surface of the wind tunnel to minimize heat loss to the surrounding environment.

Furthermore, the CO_2 evaporator and condenser were installed in separate clean rooms, which enable independent and precise control of ambient temperature and relative humidity for each heat exchanger. This arrangement provides several critical advantages for experimental investigations. Firstly, it allows the establishment of well-defined and reproducible environmental conditions for both the evaporator and condenser, which is essential for accurately evaluating thermohydraulic performance and isolating the effects of operating parameters. Secondly, the separation prevents mutual thermal interference between the evaporator and condenser, ensuring that the heat rejected by the condenser does not influence the inlet conditions of the evaporator, and vice versa. This is particularly important when investigating performance under extreme or transient operating conditions, as it maintains the integrity of measured temperature, pressure, and humidity data. Thirdly, having independent control of ambient conditions facilitates systematic parametric studies across a wide range of operating scenarios, including variations in air temperature, humidity, and flow rates, without cross-contamination or unwanted thermal coupling.

2.2. Tested finned-tube heat exchanger

Fig. 2 presents photographs of the tested finned-tube heat exchanger. The heat exchanger has dimensions of 560 mm in length and 351 mm in width. It comprises copper tubes with an outer diameter of 5 mm, wall thickness of 0.3 mm, and coil length of 560 mm. The longitudinal and transverse tube pitches are 11.2 mm and 19.5 mm, respectively. The aluminium fins have 0.1 mm thickness and 13 fins per inch. The aluminium fins are slotted in the airflow direction, with each slit measuring 1 mm in height and 1 mm in breadth in the direction of airflow. In the enhanced zone of the heat exchanger, seven such slits are incorporated per fin. The configuration consists of 2 rows and 3 circuits, with each row containing 18 coils and each circuit comprising 12 coils.

2.3. Data acquisition

During the experiments, key operating parameters were recorded, including the mass flow rate, temperature, pressure, and pressure drop of CO_2, as well as the velocity, temperature, and pressure of the cooling air, by connecting to a C series I/O data logger from National Instruments NI 9214 and visualised using LabVIEW software. The CO_2 mass flow rate was measured using a Coriolis flowmeter (KROHNE, Model Optimass MFS 3000 04). Air velocity and pressure drop were measured using a multifunction airflow meter (TSI, Model TA465). This instrument was also used to determine the pressure drop of the airflow across the tested finned-tube heat exchanger. The temperature of CO_2 was measured using Pt100 resistance temperature detectors (TC Ltd., mineral insulated with pot seal). The pressure drop of CO_2 across the finned coils was measured using an Omega differential pressure transducer (Model PX409-015DDU5V), while the absolute CO_2 pressure was measured using an Omega pressure transducer (Model PX419–1.5KGI). The outlet air was measured using a mesh of 12 copper-constantan T-type thermocouples, uniformly distributed with 145 mm spacing along the heat exchanger length and 117 mm spacing along the width. The inlet air was monitored with a separate mesh of 4 T-type thermocouples, spaced 280 mm in the length direction and 175 mm in the width direction, providing a representative average inlet temperature. This arrangement ensures precise spatial resolution of air temperature distribution, enabling accurate determination of heat transfer characteristics across the finned-tube exchanger. In addition, all sensors were calibrated according to manufacturer specifications, and data were recorded only after system stabilization. Detailed specifications of the measurement instruments are provided in Table 1.

The selection of operating ranges for CO_2 mass flow rate, air velocity, and inlet air temperature in this study is based on practical relevance, system constraints, and the need to capture representative condenser behaviour under realistic operating conditions. The chosen CO_2 mass flow rate range reflects typical values encountered in medium-scale refrigeration and heat pump systems, ensuring that the results are directly applicable to real industrial applications. The air velocity range is selected to correspond to commonly used fan operating conditions in air-cooled heat exchangers. The inlet air temperature range is chosen to represent realistic ambient conditions and to enable assessment of

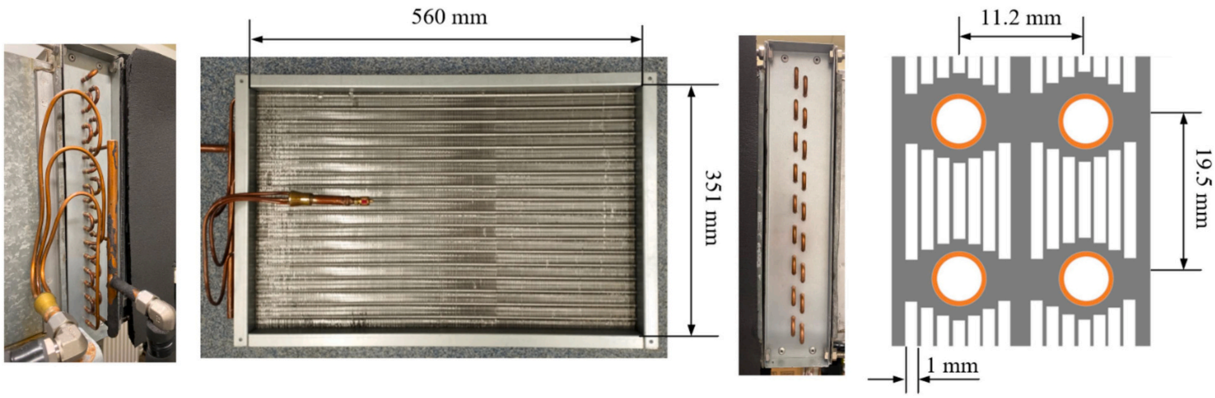

Fig. 2. Tested finned-tube heat exchanger.

Table 1
Detailed specifications of main measurement instruments used in the test facility.

Parameters	Brand	Model	Range	Accuracy
CO_2 mass flow rate	KROHNE	Optimass MFS 3000 04	0–0.5 kg/s	±0.05% of full scale
Air velocity	TSI	TA465	0–50 m/s	±3% of reading
Air pressure drop	TSI	TA465	0–3735 Pa	±1% of reading
CO_2 temperature	TC Ltd.	Pt100 mineral insulated with pot seal	−75 °C to 250 °C	±0.05 °C
Air temperature	TC Ltd.	T-type thermocouples mesh	−30 °C to 200 °C	±0.3 °C
CO_2 pressure drop	Omega	PX409-015DDU5V	0 to 15 psi	±0.08% of full scale
CO_2 pressure	Omega	Model PX419–1.5KGI	0 to 1500 psi	±0.08% of full scale

condenser performance under varying thermal driving forces and environmental influences. During the experiments, once all mass flow rates, temperatures and pressures have stabilized at the target values and have remained within the acceptable tolerance range for at least 5 min, the test run is initiated, and each experimental run is conducted over a duration of 10 min to ensure sufficient data acquisition under stable operating conditions. During this period, all relevant parameters, including temperatures, pressures, and flow rates, are continuously monitored and recorded. The use of a stabilization period prior to data collection minimizes transient effects and ensures that the measured data accurately represent steady-state system performance. During the experiments, the ambient air in the clean room housing the CO_2 evaporator was maintained at 5 °C with a relative humidity of 50%. The relative humidity of the cooling air supplied to the finned-tube condenser in the second clean room was also maintained at 50% throughout the tests. Maintaining a constant ambient relative humidity provided stable and repeatable air-side boundary conditions representative of a typical indoor laboratory environment. At 50% relative humidity, the corresponding dew-point temperature of the air was approximately −4.5 °C at 5 °C ambient temperature. The external surface temperatures of both heat exchangers remained above the dew-point temperature. Under the investigated operating conditions, no moisture condensation occurred on the air-side surfaces of either the CO_2 evaporator or the condenser. Therefore, latent heat transfer effects were negligible, and the influence of ambient humidity on the air-side heat transfer performance and pressure drop was considered insignificant.

To assess the heat losses of the experimental facility, a heat balance analysis was performed under supercritical CO_2 operating conditions, where the refrigerant remained in a single-phase gaseous state. Since the same test rig, thermal insulation, instrumentation, and measurement procedures were employed throughout all experiments, the measured heat losses are considered to be characteristics of the experimental facility rather than of a specific refrigerant operating regime. Similar validation strategies have been adopted in previous two-phase heat transfer studies, in which single-phase calibration was used to establish the thermal performance of the experimental apparatus before conducting two-phase measurements. For example, Hellenschmidt and Petagna [24] first validated their CO_2 experimental methodology under single-phase conditions by comparing the measured heat transfer performance with well-established single-phase correlations before investigating two-phase flow boiling. Similarly, Kabir [25] identified single-phase heat-loss calibration as the conventional approach widely used in two-phase flow boiling experiments for estimating heat losses and calibrating heat input prior to two-phase measurements. Therefore, although the heat balance validation was conducted under single-phase supercritical conditions, it provides confidence in the reliability of the subsequent subcritical condensation experiments.

The specific enthalpy of CO_2 can be determined directly and reliably from the measured pressure and temperature. Similarly, the heat transfer rate on the air side can be obtained directly from measured inlet and outlet air temperatures and corresponding airflow conditions.

$$\dot{Q}_{CO_2} = \dot{m}_{CO_2}\left(h_{CO_2,in} - h_{CO_2,out}\right) \tag{1}$$

$$\dot{Q}_{air} = \dot{m}_{air}\left(h_{air,out} - h_{air,in}\right) \tag{2}$$

where $\dot{m}_{CO_2}$ and $\dot{m}_{air}$ are the mass flow rate of CO_2 and cooling air, respectively. The $h_{CO_2,in}$ and $h_{CO_2,out}$ are specific enthalpies of CO_2 entering and exiting the test heat exchanger, the $h_{air,in}$ and $h_{air,out}$ are those of the cooling air, and all of them are obtained from the measured temperatures and pressures.

The relative uncertainty of heat transfer rate $\dot{Q}$ was determined using the law of propagation of uncertainties applied to its measurement equation. For the defined heat transfer rate $\dot{Q} = \dot{m}(h_{in} - h_{out}) = \dot{m}\Delta h$, the combined relative uncertainty is obtained using the root-sum-square method, assuming the input variables are independent:

$$\frac{\delta\dot{Q}}{\dot{Q}} = \sqrt{\left(\frac{\delta\dot{m}}{\dot{m}}\right)^2 + \left(\frac{\delta\Delta h}{\Delta h}\right)^2} \tag{3}$$

The uncertainty of the specific enthalpy difference Δh is itself derived from temperature and pressure measurements using thermodynamic property relations:

$$\frac{\delta \Delta h}{\Delta h} = \sqrt{\left(\frac{\delta h_{in}}{h_{in}}\right)^2 + \left(\frac{\delta h_{out}}{h_{out}}\right)^2} \tag{4}$$

$$\frac{\delta h}{h} = \sqrt{\left(\frac{\partial h}{\partial T}\right)^2 \left(\frac{\delta T}{T}\right)^2 + \left(\frac{\partial h}{\partial P}\right)^2 \left(\frac{\delta P}{P}\right)^2} \tag{5}$$

$$\frac{\partial h}{\partial T} = \frac{h(T+\Delta T, P) - h(T-\Delta T, P)}{2\Delta T} \tag{6}$$

$$\frac{\partial h}{\partial P} = \frac{h(T, P+\Delta P) - h(T, P-\Delta P)}{2\Delta P} \tag{7}$$

Based on these calculations, the relative uncertainty associated with the heat transfer rate is estimated to be within ±1% on the CO_2 side and ±3% on the cooling air side.

A comparison between the CO_2-side and air-side heat transfer rates is shown in Fig. 3. The discrepancy between the two heat transfer rates is consistently within ±5%, indicating high measurement reliability. This cross-validation approach ensures that the measured heat transfer rates are accurate and suitable for model validation and performance analysis.

3. Experimental results and discussion

Owing to the strong coupling among operating parameters, the experimental results are presented in tabular form to facilitate interpretation of the measured trends. Table 2 summarizes the condenser performance under different CO_2 mass flow rates, while Table 3 presents the results obtained at different air velocities.

Changes in CO_2 mass flow rate affect the compressor discharge state, refrigerant velocity, residence time, and flow resistance, thereby significantly influencing the condenser inlet conditions, pressure losses, and heat transfer capacity. As shown in Table 2, at a constant air velocity of 3.0 m/s and low air temperature conditions (4.6–6.0 °C), as the CO_2 mass flow rate was increased from 26.9 g/s to 35.3 g/s, the condenser inlet temperature rose from 45.5 °C to 77.3 °C, while the inlet pressure increased from 57.5 bar to 64.8 bar. The refrigerant-side pressure drop increased from 44.3 kPa to 66.5 kPa, whereas the air-side pressure drop increased only slightly from 34.0 Pa to 34.8 Pa. The heat transfer rate increased from 4.98 kW to 7.44 kW. Similar trends were observed under higher air temperature conditions (12.8–13.5 °C), where an increase in CO_2 mass flow rate from 28.6 g/s to 37.5 g/s raised the condenser inlet temperature from 47.6 °C to 81.4 °C, the inlet pressure from 61.6 bar to 69.2 bar, the refrigerant-side pressure drop from 44.2 kPa to 66.9 kPa, and the air-side pressure drop from 34.8 Pa to 36.9 Pa. Correspondingly,

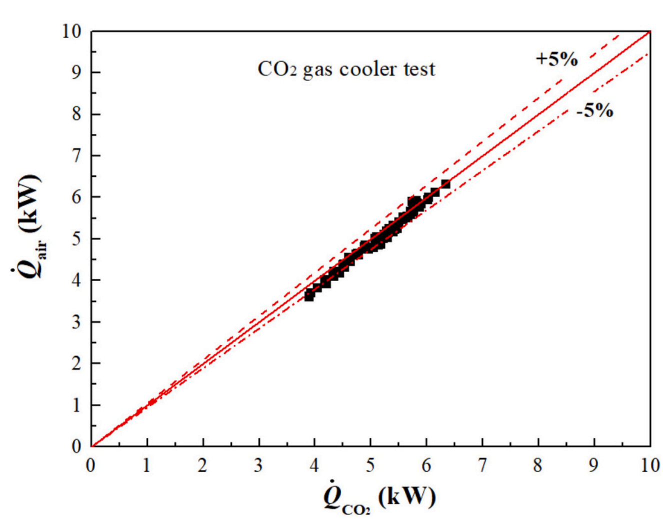

Fig. 3. Comparison of heat transfer rates between CO_2-side and air-side.

Table 2
Experimental results for different CO_2 mass flow rates.

Case	$\dot{m}_{CO_2}$, g/s	$v_{air,in}$, m/s	$T_{air,in}$, °C	$T_{CO_2,in}$, °C	$P_{CO_2,in}$, bar	ΔP_{CO_2}, kPa	ΔP_{air}, Pa	$\dot{Q}_{air}$, kW
1	26.9	3.0	4.6	45.5	57.5	44.3	34.0	4.98
2	28.6	3.0	4.6	48.9	58.5	47.8	34.0	5.45
3	30.3	3.0	5.0	53.2	59.8	53.0	34.0	5.76
4	31.5	3.0	4.8	57.0	60.6	56.0	34.0	6.06
5	32.8	3.0	5.8	62.0	62.1	58.7	34.4	6.37
6	33.6	3.0	5.7	66.4	62.7	61.2	34.4	6.61
7	34.6	3.0	5.7	71.7	63.8	64.2	34.6	7.13
8	35.3	3.0	6.0	77.3	64.8	66.5	34.8	7.44
9	28.6	3.0	12.8	47.6	61.6	44.2	34.8	3.64
10	30.3	3.0	13.0	51.8	62.9	47.8	35.0	4.03
11	31.8	3.0	12.9	56.3	64.0	51.5	35.3	4.40
12	33.0	3.0	13.1	61.1	65.2	54.7	35.7	4.75
13	34.1	3.0	13.2	65.5	66.1	55.9	36.0	5.07
14	35.0	3.0	13.2	70.6	67.0	57.4	36.3	5.48
15	35.8	3.0	13.4	76.0	67.8	60.2	36.6	5.70
16	37.5	3.0	13.5	81.4	69.2	65.9	36.9	6.28

Table 3
Experimental results for different air inlet velocities.

Case	$\dot{m}_{CO_2}$, g/s	$v_{air,in}$, m/s	$T_{air,in}$, °C	$T_{CO_2,in}$, °C	$P_{CO_2,in}$, bar	ΔP_{CO_2}, kPa	ΔP_{air}, Pa	$\dot{Q}_{air}$, kW
1	33.6	2.2	7.0	64.5	64.2	59.3	20.8	5.56
2	33.3	2.5	6.7	63.5	63.3	58.5	25.8	5.88
3	32.9	3.0	6.2	62.4	62.3	58.4	34.6	6.30
4	32.7	3.5	6.6	61.9	61.8	58.0	45.0	6.45
5	32.6	4.0	7.0	61.5	61.4	57.7	55.5	6.60
6	32.4	4.5	6.9	61.0	60.9	57.3	68.3	6.77
7	32.1	4.9	6.8	61.4	60.6	57.4	78.8	7.03
8	34.0	2.0	10.8	68.0	66.4	57.6	19.2	4.90
9	33.9	2.5	11.6	67.5	66.0	57.6	26.8	5.21
10	34.0	3.0	12.9	67.2	66.0	57.5	35.9	5.29
11	33.8	3.5	12.6	66.3	65.2	57.8	46.0	5.52
12	33.8	4.0	12.9	65.6	64.9	58.0	56.5	5.70
13	33.6	4.5	12.8	65.0	64.5	58.0	69.4	5.83
14	33.6	4.8	12.8	64.9	64.2	57.5	78.3	5.90

the heat transfer rate increased from 3.64 kW to 6.28 kW. The increase in condenser inlet temperature and pressure with increasing refrigerant mass flow rate is primarily attributed to the higher compressor work required to circulate a larger quantity of refrigerant through the system. As the mass flow rate increases, the compressor processes more CO_2 per unit time, resulting in higher discharge enthalpy and consequently higher discharge temperatures. In addition, the increased refrigerant flow rate intensifies frictional and momentum losses throughout the refrigerant circuit, requiring a higher discharge pressure to maintain the desired flow rate. The increase in refrigerant-side pressure drop is mainly attributed to the higher refrigerant velocity within the condenser tubes. Elevated flow velocities increase wall shear stress and frictional resistance, resulting in greater pressure losses along the flow path. In contrast, the air-side pressure drop exhibits only minor variations because it is primarily governed by air velocity and heat exchanger geometry, which remain unchanged during the experiments. The enhancement in heat transfer rate with increasing refrigerant mass flow rate can be attributed to several factors. First, a higher refrigerant mass flow rate increases the thermal energy transported into the condenser, thereby increasing the heat rejection potential. Second, the higher refrigerant inlet temperature increases the temperature difference between the CO_2 and the cooling air, strengthening the thermal driving force for heat transfer. Third, the increased refrigerant velocity promotes turbulent flow and enhances the internal convective heat transfer coefficient. Conversely, higher air temperatures reduce the temperature difference between the refrigerant and the cooling air, thereby weakening the thermal driving force and resulting in lower heat transfer rates under otherwise similar operating conditions.

Increasing airflow enhances heat removal from the refrigerant by improving the air-side heat transfer coefficient, while simultaneously increasing the pressure losses associated with air flow through the fin passages. As presented in Table 3, for CO_2 mass flow rates of 32.1–33.6 g/s and air temperatures of 6.2–7.0 °C, increasing the air velocity from 2.2 m/s to 4.9 m/s reduced the condenser inlet temperature from 64.5 °C to 61.4 °C and the inlet pressure from 64.2 bar to 60.6 bar. The refrigerant-side pressure drop decreased slightly from 59.3 kPa to 57.4 kPa, whereas the air-side pressure drop increased substantially from 20.8 Pa to 78.8 Pa. Correspondingly, the heat transfer rate increased from 5.56 kW to 7.03 kW. Similar trends were observed under higher air temperature conditions (10.8–12.9 °C), where CO_2 mass flow rates ranged from 33.6 g/s to 34.0 g/s. Increasing the air velocity from 2.0 m/s to 4.8 m/s decreased the condenser inlet temperature from 68.0 °C to 64.9 °C and the inlet pressure from 66.4 bar to 64.2 bar, while the refrigerant-side pressure drop remained nearly constant at 57.5–58.0 kPa. In contrast, the air-side pressure drop increased markedly from 19.2 Pa to 78.3 Pa, and the heat transfer rate increased from 4.90 kW to 5.90 kW. The increase in heat transfer rate with air velocity is primarily attributed to the enhancement of the air-side convective heat transfer coefficient, which reduces the thermal resistance on the air side and promotes more effective heat rejection from the refrigerant. Improved cooling conditions lower the refrigerant temperature throughout the condenser, resulting in reduced condenser inlet temperature and pressure. In contrast, the refrigerant-side pressure drop exhibits only minor variations because the refrigerant mass flow rate remains nearly constant, and changes in refrigerant thermophysical properties induced by enhanced cooling have a limited influence on flow resistance. The significant increase in air-side pressure drop is associated with the higher airflow resistance through the finned passages, where increased air velocity intensifies frictional and inertial losses.

4. Model development and validation

A distributed model was developed to simulate the thermohydraulic performance of CO_2 finned-tube condensers. The condenser is discretized into multiple evenly spaced segments along the flow path, which enables detailed calculation of local temperature, pressure, and flow characteristics. This segmental approach captures nonlinear variations along the condenser and provides higher fidelity compared with lumped-parameter models which cannot resolve localized thermodynamic effects. As shown in Fig. 4b, each segment is modelled as an individual cross-flow heat exchanger, allowing local variations in thermodynamic and flow properties to be captured more accurately. Within each segment, the mass quality, temperature and pressure of CO_2 and temperature and pressure of cooling air are determined through the application of energy balance equations and fluid flow resistance relationships. The heat transfer and fluid flow processes in each segment are governed by the effectiveness-NTU method [26], which enables the calculation of segmental heat transfer rates based on local inlet conditions and heat exchanger effectiveness. Pressure drop across each segment is evaluated using appropriate friction correlations, and the cumulative effect is used to determine the overall pressure loss along the tube.

For a given segment i, the heat transfer rate from the CO_2 to the cooling air is given by

$$\dot{Q}_i = \varepsilon_i C_{\mathrm{min},i}\left(T_{\mathrm{CO_2,in},i} - T_{\mathrm{air,in},i}\right) \tag{8}$$

$$\varepsilon_i = \frac{1-\exp\left[-NTU_i\left(1-C_i^*\right)\right]}{1-C_i^*\exp\left[-NTU_i\left(1-C_i^*\right)\right]} \tag{9}$$

$$C_i^* = \frac{C_{\mathrm{min},i}}{C_{\mathrm{max},i}} \tag{10}$$

$$C_{\mathrm{min},i} = \min\left(\dot{m}_{\mathrm{air},i}c_{\mathrm{pair},i}, \dot{m}_{\mathrm{CO_2},i}c_{\mathrm{pCO_2},i}\right) \tag{11}$$

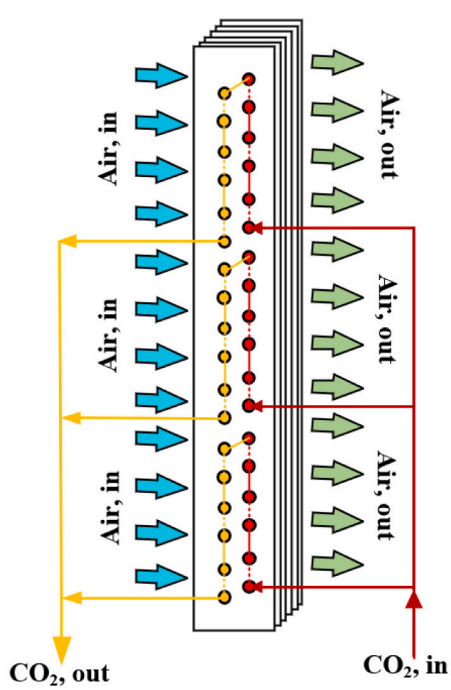

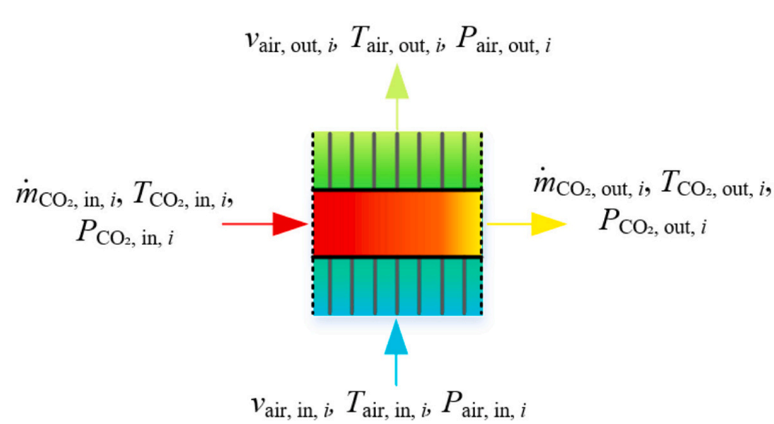

Fig. 4. Model of CO_2 finned-tube condenser. (a) Whole heat exchanger and (b) each segment.

$$C_{\max,i} = \max\left(\dot{m}_{\text{air},i}c_{\text{pair},i}, \dot{m}_{CO_2,i}c_{pCO_2,i}\right) \tag{12}$$

$$NTU_i = \frac{U_iA_i}{C_{\min,i}} \tag{13}$$

$$U_iA_i = \frac{1}{\frac{1}{h_{CO_2,i}A_{CO_2,i}} + R_{t,i} + \frac{1}{h_{\text{air},i}A_{\text{air},i}\eta_{\text{air},i}}} \tag{14}$$

where $\dot{Q}$, ε, C, NTU and U denote the heat transfer rate, heat exchanger effectiveness, heat capacity rate, number of transfer unit and overall heat transfer coefficient, respectively. T, $\dot{m}$, h, A, R and η represent the temperature, mass flow rate, heat transfer coefficient, heat transfer area, thermal resistance through the tube and surface efficiency of a finned tube, respectively.

The CO_2-side heat transfer coefficient and frictional pressure drop are evaluated using different correlations depending on the local flow regime within the condenser. Unlike previous work by Chai et al. [9], which focused on single-phase supercritical gas coolers, the present study addresses subcritical condensation with phase-change phenomena, requiring fundamentally different model treatment and enabling prediction of latent heat-dominated heat transfer processes. In the two-phase condensation region, the heat transfer coefficient is calculated using the correlation proposed by Shah [27], which accounts for the effects of mass flux, vapour quality, and thermophysical properties, and is widely validated for predicting CO_2 condensation in channels under high-pressure conditions. The two-phase frictional pressure drop is determined using the Chisholm correlation [28], which incorporates both liquid and vapour phase contributions and accounts for momentum and frictional effects in two-phase flow. In the single-phase superheated gas region, the CO_2 convective heat transfer coefficient is calculated using the Gnielinski correlation [29], which is applicable for turbulent flow in smooth tubes and includes the influence of Reynolds number and Prandtl number. In addition, the Petukhov–Kirillov correlation [30] is used to evaluate the friction factor under turbulent single-phase flow conditions, ensuring accurate prediction of pressure losses in the superheated region. By combining Shah and Chisholm correlations for the two-phase region with Gnielinski and Petukhov–Kirillov correlations for the single-phase superheated region, the model provides a consistent and physically based description of both thermal and hydraulic behaviours of CO_2 across different thermodynamic states. These state-dependent correlations improve the robustness and predictive accuracy of the distributed condenser model. The heat transfer and pressure drop characteristics of the cooling air flowing across the finned-tube heat exchanger are evaluated using the empirical correlations proposed by Wang et al. [31], which are specifically developed for finned-tube heat exchangers. The fin efficiency is evaluated using the approximation method proposed by Schmidt [32], which is widely applied for finned-tube heat exchangers due to its simplicity and reasonable accuracy. The heat transfer and friction factor correlations employed in the CO_2 finned-tube condenser model are summarized in Appendix A.

During the calculation, the model requires only the inlet properties of CO_2 and cooling air, while outlet properties are obtained through two nested iterative routines. The inside iteration adjusts the segmental tube wall temperature until the heat transfer rates predicted from the CO_2 and air sides converge, ensuring energy balance and accounting for wall thermal resistance. The outside iteration adjusts the CO_2 outlet mass quality incrementally to satisfy the overall inlet temperature boundary condition, enabling global convergence while maintaining segmental accuracy. Segmental heat transfer rates and pressure drops are calculated sequentially, and cumulative pressure drops are used to determine total condenser resistance. This methodology captures coupled thermal and hydraulic interactions along the finned-tube condenser, accounting for the nonlinear dependencies of CO_2 thermophysical properties in the subcritical cycle. As shown in Fig. 5, the flowchart provides a clear schematic of these steps, showing the sequential calculation of

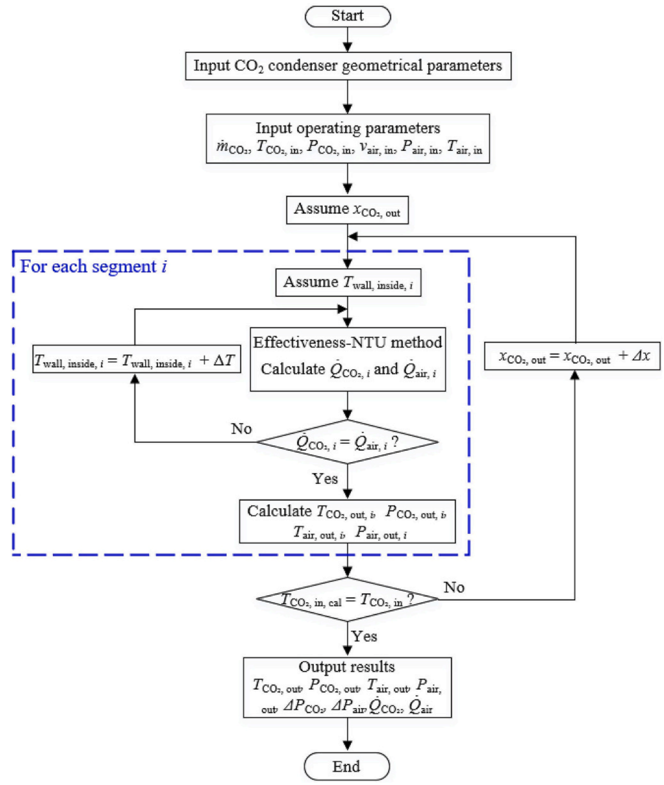

Fig. 5. Flow chart of CO_2 finned-tube condenser model.

segmental heat transfer and pressure drop, the inside iteration for wall temperature convergence, and the outside iteration for mass quality adjustment. CO_2 thermophysical properties including density, specific heat capacity, thermal conductivity and dynamic viscosity, were obtained from the NIST REFPROP v10.1 database based on the local temperature and pressure. REFPROP employs high-accuracy real-fluid equations of state and transport-property models, enabling accurate representation of the non-ideal thermodynamic behaviour of CO_2 over a wide range of operating conditions. The use of a real-gas thermophysical model is particularly important in high-pressure and near-critical applications, where ideal-gas assumptions may lead to significant deviations in the prediction of thermodynamic properties, phase equilibrium, and transport processes [21,33].

In the present modelling approach, the condenser is assumed to operate under steady-state conditions, with all system variables remaining constant over time. Heat exchange between the condenser and the surrounding environment is neglected, implying that all heat transfer occurs solely between the refrigerant and the cooling air. Axial heat conduction along the tube wall and within the fins is assumed to be negligible compared to convective heat transfer. These simplifications reduce computational complexity while maintaining sufficient accuracy for predicting the overall thermohydraulic performance of the finned-tube condenser. Each condenser tube is discretised into 20 equal segments along the refrigerant flow direction. The selection of 20 segments is based on a segment independence analysis. Additional simulations were conducted with higher segment numbers (e.g., 30, 40, and 50 segments), and the results showed negligible variations in predicted heat transfer rate and pressure drop (within $\pm 1\%$).

The accuracy of the distributed CO_2 finned-tube condenser model was evaluated by comparing predicted heat transfer rates and pressure drops with experimental measurements under 30 distinct operating conditions, as summarized in Tables 2 and 3. Fig. 6 presents the comparison of total heat transfer rates, showing that model predictions deviate by less than 10% from the experimental values across all

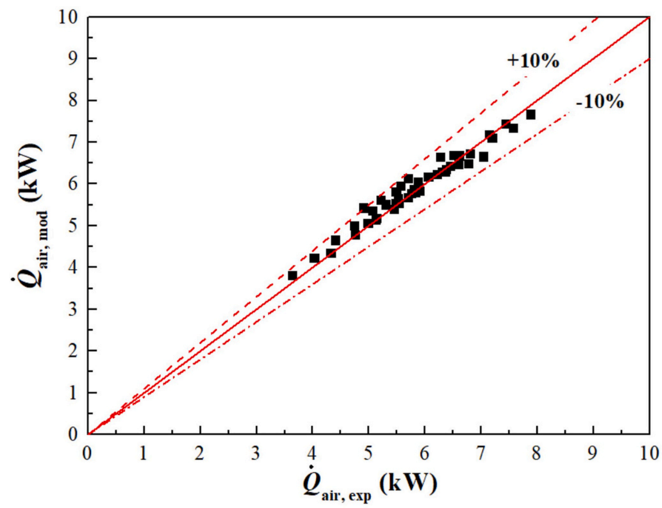

Fig. 6. Comparison of heat transfer rate between model prediction and experimental measurement.

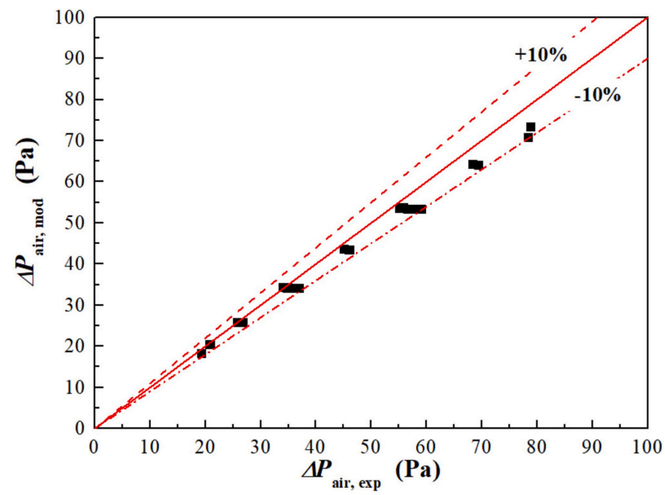

Fig. 8. Comparison of air pressure drop between model prediction and experimental measurement.

conditions. This close agreement indicates that the distributed effectiveness-NTU model, in conjunction with the applied segmental heat transfer correlations, reliably captures the energy transport processes within the condenser, including the effects of variations in CO_2 mass flow rate, air velocity, and inlet temperatures.

The comparison of CO_2-side pressure drops, shown in Fig. 7, demonstrates that predicted values remain within ±15% of the measured data for all operating points. The slightly larger deviations compared to heat transfer are attributed to the sensitivity of two-phase pressure drop to local flow patterns, tube friction, and flow regime transitions, which are inherently approximated through empirical correlations. Nonetheless, the model effectively reproduces the overall hydraulic behaviour of the refrigerant, confirming its capability for accurate prediction of segmental pressure drops. For the air-side pressure drop, Fig. 8 shows that predicted values are within ±10% of experimental measurements across the tested conditions. This agreement validates the correlations used for convective heat transfer and airflow resistance on finned surfaces.

5. Model results and discussion

The model results are presented graphically to illustrate the influence of key operating parameters on condenser thermohydraulic performance. The effects of CO_2 mass flow rate on the condenser thermohydraulic performance are illustrated by Figs. 9 and 10. The variations in heat transfer rate and outlet mass quality are presented in Fig. 9, while Fig. 10 shows the corresponding refrigerant-side and air-side pressure drops. For a CO_2 inlet temperature of 65.0 °C, inlet pressure of 65.0 bar, air velocity of 3.0 m/s, and air inlet temperature of 13.0 °C, an increase in CO_2 mass flow rate from 25.0 g/s to 40.0 g/s increased the heat transfer rate by 21.1%, from 4.54 kW to 5.50 kW. Simultaneously, the outlet mass quality increased from 0.23 to 0.61, indicating a higher outlet vapour quality. This behaviour is attributed to the reduced refrigerant residence time within the condenser at higher mass flow rates, which limits the extent of condensation despite the increase in heat transfer rate. The refrigerant-side pressure drop increased significantly from 36.6 kPa to 74.0 kPa due to the higher flow velocity and associated frictional losses within the tubes. In contrast, the air-side pressure drop remained constant at 34.2 Pa because the air velocity was maintained at a fixed value.

The predicted local distributions of CO_2 temperature and heat transfer coefficient provide detailed insight into the evolution of thermal resistance and condensation behaviour along the flow path. These profiles are essential for identifying regions of enhanced heat transfer, evaluating the physical consistency of the model, and improving the

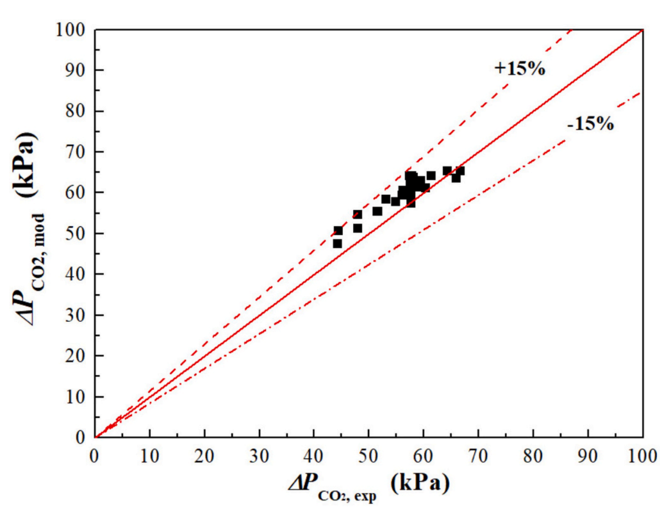

Fig. 7. Comparison of CO_2 pressure drop between model prediction and experimental measurement.

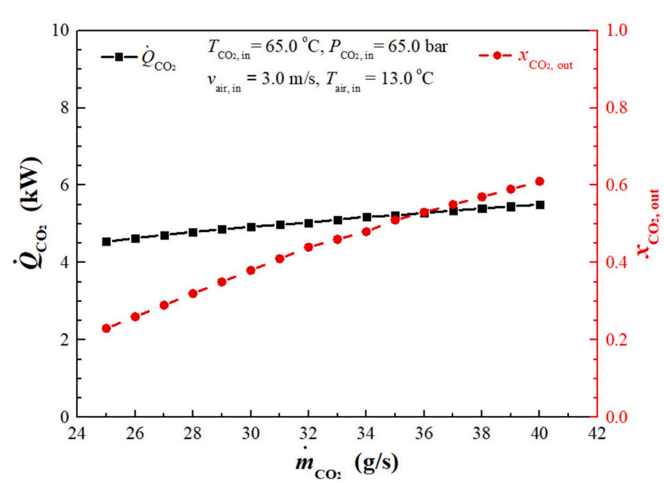

Fig. 9. Variations of heat transfer rate and outlet mass quality with CO_2 mass flow rate.

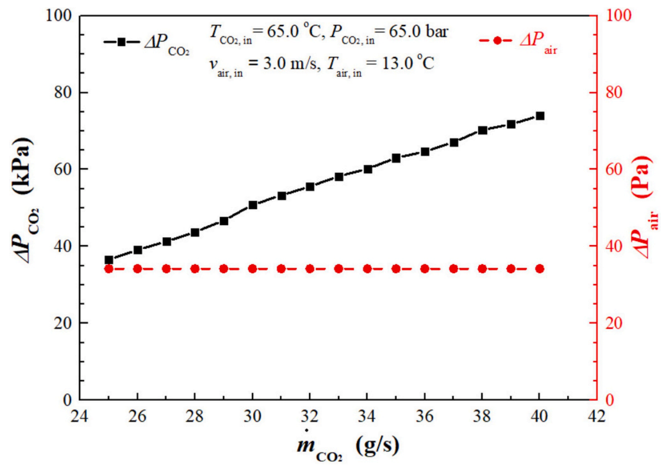

Fig. 10. Variations of CO_2 pressure drop and air pressure drop with CO_2 mass flow rate.

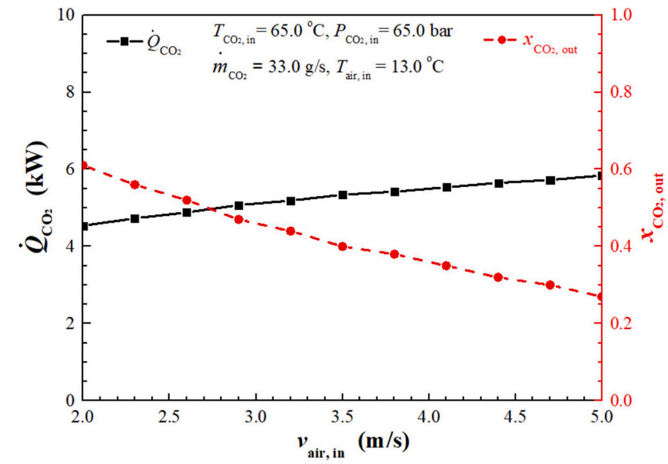

Fig. 12. Variations of heat transfer rate and outlet mass quality with air velocity.

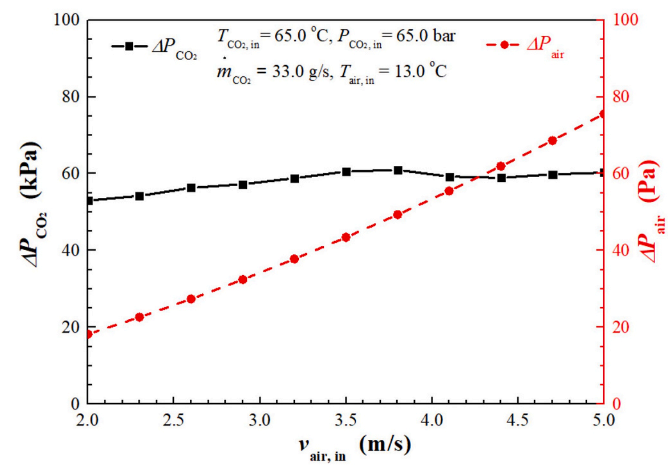

Fig. 13. Variations of CO_2 pressure drop and air pressure drop with air velocity.

understanding of local condensation mechanisms, thereby supporting performance optimisation. Fig. 11 illustrates the axial variation of local CO_2 temperature and local heat transfer coefficient along the tube length for CO_2 mass flow rates ranging from 25.0 g/s to 40.0 g/s. $L_{CO_2,x}$ is the local tube length measured along the CO_2 flow direction. Along the flow direction, the CO_2 temperature decreases from 65.0 °C at the inlet to the saturation temperature of approximately 25.5 °C. Higher refrigerant mass flow rates result in higher temperatures in the upstream superheated region because of reduced residence time, despite enhanced local heat transfer coefficients. In contrast, the local heat transfer coefficient initially increases along the tube in the superheated region and reaches a pronounced peak in the saturated region, where intensified convection and phase-change heat transfer occur. With increasing mass flow rate, this peak shifts downstream and increases in magnitude, from 6.3 kW/(m^2·K) at 25.0 g/s to 9.2 kW/(m^2·K) at 40.0 g/s, indicating enhanced local heat transfer under higher refrigerant velocities.

The influence of air velocity on the condenser thermohydraulic performance is presented in Figs. 12 and 13. For a CO_2 inlet temperature of 65.0 °C, inlet pressure of 65.0 bar, mass flow rate 33.0 g/s, and air inlet temperature of 13.0 °C, increasing the air velocity from 2.0 m/s to 5.0 m/s enhances the air-side convective heat transfer coefficient, thereby reducing the overall thermal resistance and increasing the total heat transfer rate from 4.54 kW to 5.84 kW. This improved heat rejection capacity promotes more extensive condensation of CO_2, leading to a reduction in outlet vapour quality from 0.61 to 0.27. The higher air velocity strengthens forced convection over the finned surfaces, increasing the temperature gradient between the refrigerant and air and accelerating phase change. In terms of pressure losses, the air-side pressure drop increases significantly and approximately linearly from 18.2 Pa to 75.5 Pa due to elevated frictional effects within the fin passages at higher flow rates. In contrast, the CO_2 pressure drop shows only a weak dependence on air velocity, varying slightly between 53.0 kPa and 61.0 kPa and tending to stabilise at approximately 60.0 kPa. This weak sensitivity is attributed to the fact that refrigerant-side flow conditions are primarily governed by mass flux and thermophysical properties, which are not directly affected by changes in external air flow rate.

Fig. 14 presents the variation of local CO_2 temperature and heat transfer coefficient for air velocities of 2.0 m/s, 3.5 m/s, and 5.0 m/s. The CO_2 temperature decreases along the tube from 65.0 °C to approximately 25.5 °C, with higher air velocities accelerating the cooling process due to enhanced air-side convective heat transfer and reduced thermal resistance. The local heat transfer coefficient increases along the flow direction and attains a maximum value of approximately 7.8 kW/(m^2·K), reflecting the transition from superheated to two-phase flow and intensified phase-change heat transfer. With higher air velocity, this peak shifts upstream, indicating earlier onset of effective condensation and stronger local convective interaction near the condenser inlet, driven by higher air-side heat transfer coefficients.

The influence of inlet air temperature on the thermohydraulic

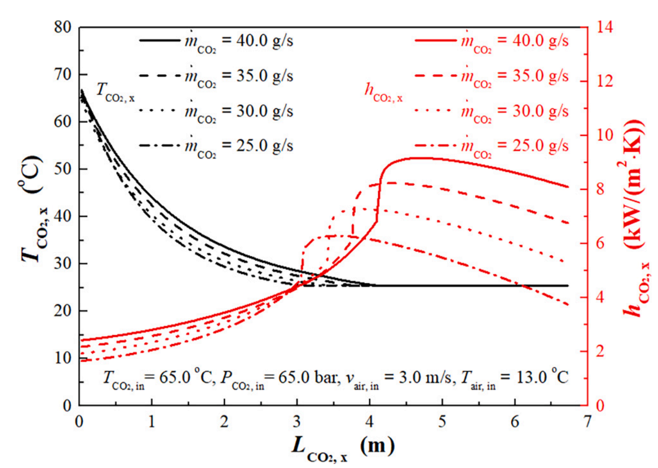

Fig. 11. Local CO_2 temperature and heat transfer coefficient for different CO_2 mass flow rates.

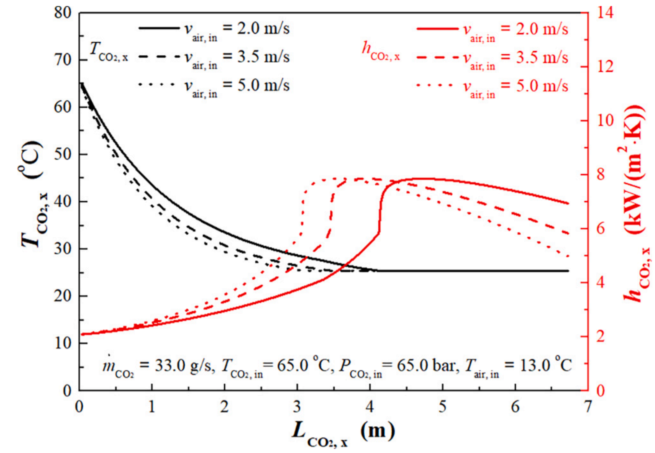

Fig. 14. Local CO_2 temperature and heat transfer coefficient for different air velocities.

performance of the CO_2 condenser is presented in Figs. 15 and 16. For a CO_2 inlet temperature of 65.0 °C, inlet pressure of 65.0 bar, mass flow rate 33.0 g/s, and air velocity 3.5 m/s, as the inlet air temperature increases from 7.0 °C to 20.0 °C, the reduced thermal driving force between CO_2 and air progressively weakens convective heat transfer, leading to a decline in the total heat transfer rate from 6.84 kW to 3.54 kW. This reduction directly affects the condensation process, resulting in an increase in outlet vapour quality from 0.01 to 0.87, which reflects a transition from nearly complete condensation at low air temperatures to seriously incomplete condensation at higher air temperatures due to insufficient heat rejection within the available surface area and residence time. The air-side pressure drop remains nearly constant at approximately 43.5 Pa because the airflow rate and heat exchanger geometry are unchanged, and therefore aerodynamic resistance is unaffected by thermal boundary conditions. In contrast, the CO_2 pressure drop shows a weak non-monotonic behaviour, increasing slightly from 56.4 kPa at 7.0 °C to 59.9 kPa at 13.0 °C before decreasing to 43.4 kPa at 20.0 °C. This trend is attributed to the coupled effects of temperature-dependent refrigerant properties and phase distribution. At lower air temperatures, enhanced condensation increases liquid fraction and frictional resistance, while at higher air temperatures reduced condensation intensity leads to a predominantly vapour-phase flow with lower density and viscosity, thereby decreasing pressure losses.

Fig. 17 presents the variation of local CO_2 temperature and heat transfer coefficient for inlet air temperatures of 7.0 °C, 13.0 °C, and 19.0 °C. A lower inlet air temperatures promote faster cooling due to a larger local temperature driving force, which enhances convective heat transfer and accelerates condensation. The local heat transfer coefficient increases along the flow direction and reaches a maximum value of approximately 7.8 kW/(m^2·K), corresponding to the transition from superheated to two-phase flow. With decreasing inlet air temperature, this peak shifts upstream, indicating an earlier initiation of phase-change heat transfer and a shortened superheated region because of intensified external cooling conditions.

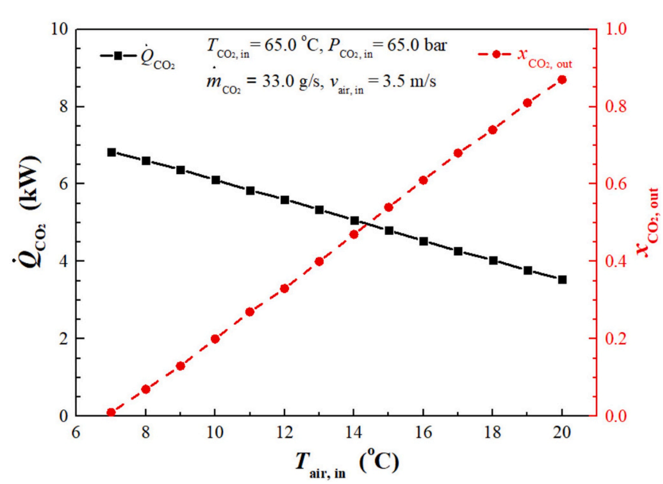

Fig. 15. Variations of heat transfer rate and outlet mass quality with inlet air temperature.

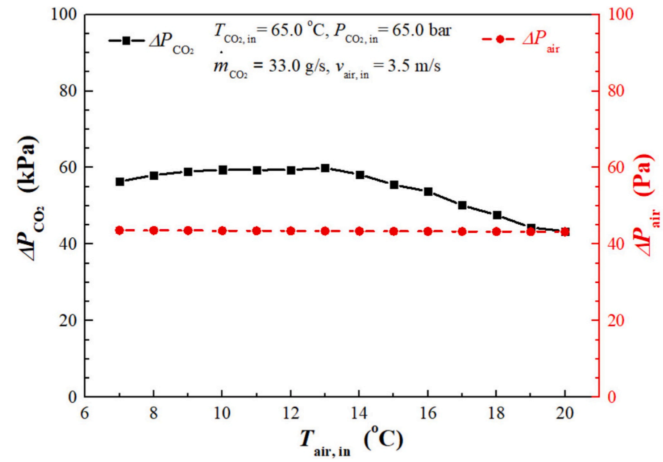

Fig. 16. Variations of CO_2 pressure drop and air pressure drop with inlet air temperature.

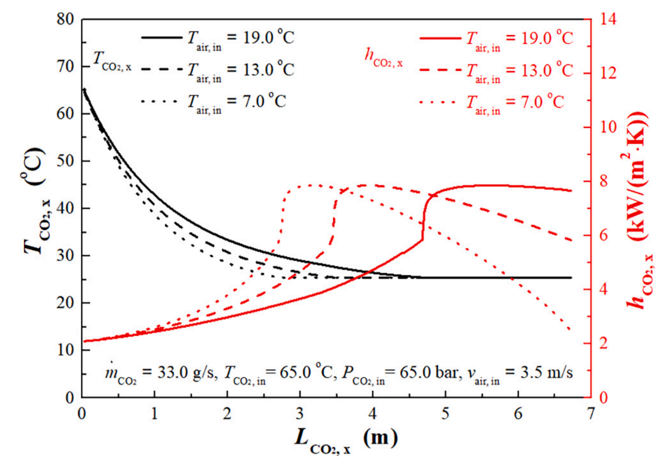

Fig. 17. Local CO_2 temperature and heat transfer coefficient for different inlet air temperatures.

6. Conclusions

This study presented a combined experimental and numerical investigation of the thermohydraulic performance of a CO_2 finned-tube condenser operating under subcritical conditions. A distributed segment-by-segment effectiveness–NTU model was developed and validated using extensive experimental measurements. The main conclusions are as follows:

- The thermohydraulic performance of the CO_2 finned-tube condenser is strongly influenced by refrigerant mass flow rate, air velocity, and inlet air temperature. Increasing the CO_2 mass flow rate enhanced heat transfer owing to greater thermal energy transport and higher refrigerant-side heat transfer coefficients. However, the associated increase in refrigerant velocity resulted in higher refrigerant-side pressure losses. Increasing air velocity improved heat rejection and promoted more complete condensation by reducing the dominant air-side thermal resistance, although this benefit was accompanied by a substantial increase in air-side pressure drop. In contrast, elevated inlet air temperatures reduced the thermal driving force for heat transfer, resulting in lower heat transfer rates and incomplete condensation.

- The developed distributed model successfully captured the coupled heat transfer, phase-change, and pressure-drop processes occurring in both the superheated and two-phase regions of the condenser. Validation against 30 operating conditions demonstrated deviations within ±10% for heat transfer rate, ±15% for refrigerant-side pressure drop, and ±10% for air-side pressure drop, confirming the robustness and predictive capability of the modelling approach.
- Model predictions revealed detailed local thermohydraulic behaviour that is difficult to obtain experimentally. The refrigerant temperature decreased progressively from the superheated region to the saturation temperature, while the local heat transfer coefficient increased sharply upon entering the condensation region. The highest heat transfer coefficients occurred within the two-phase region and were strongly affected by operating conditions. Increasing the refrigerant mass flow rate shifted the location of the peak heat transfer coefficient downstream, whereas increasing air velocity or reducing inlet air temperature shifted the peak upstream, indicating an earlier onset of condensation and enhanced local heat transfer.
- The combination of high-quality experimental measurements and validated distributed modelling provides a reliable framework for analysing and optimising subcritical CO_2 finned-tube condensers. The proposed methodology can support the design of high-efficiency refrigeration and heat pump systems and can be extended to alternative heat exchanger geometries and operating conditions. Future work will focus on extending the model to a wider range of condenser geometries and operating conditions, including trans-critical applications, to further enhance its applicability and generality.

Declaration of competing interest

The authors declare that they have no known competing financial interests or personal relationships that could have appeared to influence the work reported in this paper.

Acknowledgements

This research received funding from the Engineering and Physical Sciences Research Council (EPSRC) of the UK under research grants EP/P004636/1 – OPTEMIN, EP/V001795/1 – SCOTWOHR and the European Union's Horizon 2020 research and innovation program under grant agreement No. 680599 – I-ThERM and Grant Agreement No. 101022831 – CO2OLHEAT and the support from Brunel Research Culture Seed Fund No. 13157. All data used are in the paper but if any additional information is required it can be obtained by contacting the corresponding author.

Appendix A. Heat transfer and friction factor correlations employed in the CO_2 finned-tube condenser model.

The two-phase condensation heat transfer coefficient is calculated using the correlation proposed by Shah [27].

$$h_{\mathrm{TP}} = \begin{cases} h_{\mathrm{I}} \text{ when } J_g > 0.98(Z+0.263)^{-0.62} \\ h_{\mathrm{I}} + h_{\mathrm{Nu}} \text{ when } 0.98(Z+0.263)^{-0.62} < J_g < 0.95\left(1.254+2.27Z^{1.249}\right)^{-1} \\ h_{\mathrm{Nu}} \text{ when } J_g < 0.95\left(1.254+2.27Z^{1.249}\right)^{-1} \end{cases} \tag{A.1}$$

$$h_{\mathrm{I}} = h_{\mathrm{LO}}\left(1+\frac{3.8}{Z^{0.95}}\right)\left(\frac{\mu_{\mathrm{L}}}{\mu_{\mathrm{G}}}\right) \tag{A.2}$$

$$h_{\mathrm{Nu}} = 1.32\mathrm{Re}_{\mathrm{LO}}^{-1/3}\left(\frac{\rho_{\mathrm{L}}(\rho_{\mathrm{L}}-\rho_{\mathrm{G}})gk_{\mathrm{L}}^3}{\mu_{\mathrm{L}}^2}\right)\left(\frac{\mu_{\mathrm{L}}}{\mu_{\mathrm{G}}}\right) \tag{A.3}$$

$$h_{\mathrm{LO}} = \frac{0.023\mathrm{Re}_{\mathrm{LO}}^{0.8}\mathrm{Pr}_{\mathrm{L}}^{0.4}k_{\mathrm{L}}}{D} \tag{A.4}$$

$$Z = \left(\frac{1}{x}-1\right)^{0.8}\mathrm{Pr}_{\mathrm{L}}^{0.4} \tag{A.5}$$

$$J_g = \frac{xG}{\left(gD\rho_{\mathrm{G}}(\rho_{\mathrm{L}}-\rho_{\mathrm{G}})\right)^{0.5}} \tag{A.6}$$

where h is the heat transfer coefficient, ρ, μ, and k respectively are the density, viscosity and thermal conductivity, Re and Pr denote the Reynold number and Prandtl number, D is the inside diameter of tube, g is the acceleration due to gravity, x is the vapour quality and G is the mass flux. The subscripts TP, L, G and LO respectively mean two-phase, liquid phase, vapour phase and liquid phase flowing alone in the tube.

The two-phase frictional pressure drop is determined using the Chisholm correlation [28].

$$\left(\frac{dP}{dz}\right)_{\mathrm{TP}} = \phi_{\mathrm{L}}^2\left(\frac{dP}{dz}\right)_{\mathrm{L}} \tag{A.7}$$

$$\phi_{\mathrm{L}}^2 = 1+\frac{C}{X}+\frac{1}{X^2} \tag{A.8}$$

$$X = \left[\frac{\left(\frac{dP}{dz}\right)_L}{\left(\frac{dP}{dz}\right)_V} \right]^{1/2} \tag{A.9}$$

where $\left(\frac{dP}{dz}\right)_{TP}$, $\left(\frac{dP}{dz}\right)_L$ and $\left(\frac{dP}{dz}\right)_V$ are the two-phase, the single-phase liquid and gas pressure gradients, respectively, ϕ_L^2 is the Lockhart-Martinelli two-phase multiplier. The parameter C depends on the flow regime and is typically selected based on the combination of laminar or turbulent flow in each phase.

The superheated single-phase heat transfer coefficient is calculated using the Gnielinski correlation [29] and friction factor is calculated by the Petukhov–Kirillov correlation [30].

$$\mathrm{Nu} = \frac{(f/8)(\mathrm{Re} - 1000)\mathrm{Pr}}{1 + 12.7(f/8)^{1/2}(\mathrm{Pr}^{2/3} - 1)} \tag{A.10}$$

$$f = (0.790\ln\mathrm{Re} - 1.64)^{-2} \tag{A.11}$$

The heat transfer and pressure drop of cooling air flowing across the finned-tube heat exchanger are calculated using the correlations proposed by Wang et al. [31].

$$j = \begin{cases} 0.9047\mathrm{Re}_{\mathrm{Dc}}^{j_1}\left(\frac{F_s}{D_c}\right)^{j_2}\left(\frac{P_t}{P_l}\right)^{j_3}\left(\frac{S_s}{S_h}\right)^{-0.0305} N^{0.0782} \text{ for } N > 2 \text{ and } \mathrm{Re}_{\mathrm{Dc}} < 700 \\ 1.0691\mathrm{Re}_{\mathrm{Dc}}^{j_4}\left(\frac{F_s}{D_c}\right)^{j_5}\left(\frac{S_s}{S_h}\right)^{j_6} N^{j_7} \text{ for } N = 1,2 \text{ or } N > 2 \text{ and } \mathrm{Re}_{\mathrm{Dc}} > 700 \end{cases} \tag{A.12}$$

$$f = 1.201\mathrm{Re}_{\mathrm{Dc}}^{f_1}\left(\frac{F_s}{D_c}\right)^{f_2}\left(\frac{P_t}{P_l}\right)^{f_3}\left(\frac{S_s}{S_h}\right)^{f_4} N^{f_5} S_n^{f_6} \tag{A.13}$$

In these correlations, j_1–j_7 and f_1–f_7 are empirical coefficients that depend on the specific fin geometry and are obtained through regression of experimental data.

$$j_1 = -0.2555 - \frac{0.0312}{(F_s/D_c)} - 0.0487N \tag{A.14}$$

$$j_2 = 0.9703 - 0.0455\sqrt{\mathrm{Re}_{D_c}} - 0.4986\left(\ln\frac{P_t}{P_l}\right)^2 \tag{A.15}$$

$$j_3 = 0.2405 - 0.003Re + 5.5349\left(\frac{F_s}{D_c}\right) \tag{A.16}$$

$$j_4 = -0.535 + 0.017\left(\frac{P_t}{P_l}\right) - 0.0107N \tag{A.17}$$

$$j_5 = 0.4115 + 5.5756\sqrt{\frac{N}{\mathrm{Re}_{D_c}}}\ln\frac{N}{\mathrm{Re}_{D_c}} + 24.2028\sqrt{\frac{N}{\mathrm{Re}_{D_c}}} \tag{A.18}$$

$$j_6 = 0.2446 + 1.0491\left(\frac{S_s}{S_h}\right)\ln\frac{S_s}{S_h} - 0.216\left(\frac{S_s}{S_h}\right)^3 \tag{A.19}$$

$$j_7 = 0.3749 + 0.0046\sqrt{\mathrm{Re}_{D_c}}\ln\mathrm{Re}_{D_c} - 0.0433\sqrt{\mathrm{Re}_{D_c}} \tag{A.20}$$

$$f_1 = -0.1401 + 0.2567\ln\left(\frac{F_s}{D_c}\right) + 4.399e^{-S_n} \tag{A.21}$$

$$f_2 = -0.383 + 0.7998\ln\left(\frac{F_s}{D_c}\right) + \frac{5.1772}{S_n} \tag{A.22}$$

$$f_3 = -1.7266 - 0.1102\ln\mathrm{Re}_{D_c} - 1.4501\left(\frac{F_s}{D_c}\right) \tag{A.23}$$

$$f_4 = 0.4034 - 0.199\frac{(S_s/S_h)}{\ln(S_s/S_h)} + 0.4208\frac{\ln(S_s/S_h)}{(S_s/S_h)^2} \tag{A.24}$$

$$f_5 = -9.0566 + 0.6199\ln\mathrm{Re}_{D_c} + \frac{32.8057}{\ln(\mathrm{Re}_{D_c})} - \frac{0.2881}{\ln N} + \frac{0.9583}{N^{1.5}} \tag{A.25}$$

$$f_6 = -1.4994 + 1.209\left(\frac{P_t}{P_l}\right) + \frac{1.4601}{S_n} \tag{A.26}$$

The geometric parameters incorporated into the correlations include the fin spacing (F_s), fin collar outside diameter (D_c), transverse tube pitch (P_t), and longitudinal tube pitch (P_l), which collectively define the structural arrangement of the finned-tube bundle. In addition, for enhanced fin surfaces, parameters such as slit breadth in the airflow direction (S_s), slit height (S_h), number of tube rows (N), and number of slits in an enhanced zone (S_n) are included to account for the influence of fin modifications on airflow disturbance and heat transfer enhancement. Re_{D_c} is the Reynolds number based on tube collar diameter.

Data availability

Data will be made available on request.

References

[1] S.M.R. Bantillo, G.A.C. Callejo, S.M.K.G. Camacho, M.A. Montalban, R.E. Valderin, R.V.C. Rubi, Future trends of natural refrigerants: selection, preparation, and evaluation, Eng. Proc. 67 (1) (2024) 9, https://doi.org/10.3390/engproc2024067009.
[2] Y. Song, C. Cui, X. Yin, F. Cao, Advanced development and application of transcritical CO_2 refrigeration and heat pump technology—a review, Energy Rep. 8 (2022) 7840–7869, https://doi.org/10.1016/j.egyr.2022.05.233.
[3] Y. Wang, S. Zong, Y. Song, F. Cao, Y. He, Q. Gao, Experimental and techno-economic analysis of transcritical CO_2 heat pump water heater with fin-and-tube and microchannel heat exchanger, Appl. Therm. Eng. 199 (2021) 117606, https://doi.org/10.1016/j.applthermaleng.2021.117606.
[4] Y. Chen, Y. Song, H. Xie, M. Yang, F. Cao, X. Pang, Experimental comparison between finned-tube and micro-channel heat exchangers in a transcritical CO_2 air-conditioning and heat pump system used in rail vehicles, Appl. Therm. Eng. 297 (2026) 130795, https://doi.org/10.1016/j.applthermaleng.2026.130795.
[5] L. Huang, V. Aute, R. Radermacher, A model for air-to-refrigerant microchannel condensers with variable tube and fin geometries, Int. J. Refrig. 40 (2014) 269–281, https://doi.org/10.1016/j.ijrefrig.2014.01.001 40.
[6] X.Y. Zhang, Y.T. Ge, J.N. Sun, Performance analysis of finned-tube CO_2 gas cooler with advanced 1D-3D CFD modelling development and simulation, Appl. Therm. Eng. 176 (2020) 115421, https://doi.org/10.1016/j.applthermaleng.2020.115421.
[7] R.L. Webb, Air-side heat transfer in finned tube heat exchangers, Heat Transfer Eng. 1 (1980) 33–49, https://doi.org/10.1080/01457638008939561.
[8] Y. Maghsoudali, A. Rastegarkoutenaei, M. Sahami, M.G. Bandpy, Experimental investigating the thermal and hydraulic performance of heat exchangers with helix wire finned tube, Appl. Therm. Eng. 231 (2023) 120919, https://doi.org/10.1016/j.applthermaleng.2023.120919.
[9] L. Chai, K.M. Tsamos, S.A. Tassou, Modelling and evaluation of the thermohydraulic performance of finned-tube supercritical carbon dioxide gas coolers, Energies 13 (5) (2020) 1031, https://doi.org/10.3390/en13051031.
[10] K.M. Tsamos, Y.T. Ge, I. Santosa, S.A. Tassou, Experimental investigation of gas cooler/condenser designs and effects on a CO_2 booster system, Appl. Energy 186 (2017) 470–479, https://doi.org/10.1016/j.apenergy.2016.03.004.
[11] I.M.C. Santosa, B.L. Gowreesunker, S.A. Tassou, K.M. Tsamos, Y.T. Ge, Investigations into air and refrigerant side heat transfer coefficients of finned-tube CO_2 gas coolers, Int. J. Heat Mass Transf. 107 (2017) 168–180, https://doi.org/10.1016/j.ijheatmasstransfer.2016.11.011.
[12] A. Vojacek, V. Dostal, F. Goettelt, M. Rohde, T. Melichar, Performance test of the air-cooled finned-tube supercritical CO_2 sink heat exchanger, J. Thermal Sci. Eng. Appl. 11 (3) (2019) 031014, https://doi.org/10.1115/1.4041686.
[13] X. Zhang, Y.T. Ge, The effect of heat conduction through fins on the performance of finned-tube CO_2 supercritical gas coolers, Int. J. Heat Mass Transf. 181 (2021) 121908, https://doi.org/10.1016/j.ijheatmasstransfer.2021.121908.
[14] Y.T. Ge, R.T. Cropper, Simulation and performance evaluation of finned-tube CO_2 gas coolers for refrigeration systems, Appl. Therm. Eng. 29 (5–6) (2009) 957–965, https://doi.org/10.1016/j.applthermaleng.2008.05.013.
[15] C. Alexopoulos, O. Aljolani, F. Heberle, T.C. Roumpedakis, D. Brüggemann, S. Karellas, Design evaluation for a finned-tube CO_2 gas cooler in residential applications, Energies 13 (10) (2020) 2428, https://doi.org/10.3390/en13102428.
[16] X. Zhang, Y. Ge, J. Sun, CFD performance analysis of finned-tube CO_2 gas coolers with various inlet air flow patterns, Energy and Built Environment 1 (3) (2020) 233–241, https://doi.org/10.1016/j.enbenv.2020.02.004.
[17] X.Y. Zhang, Y.T. Ge, J.N. Sun, Performance analysis of finned-tube CO_2 gas cooler with advanced 1D-3D CFD modelling development and simulation, Appl. Therm. Eng. 176 (2020) 115421, https://doi.org/10.1016/j.applthermaleng.2020.115421.
[18] J. Zhou, X. Li, J. Feng, X. Xu, L. Zhang, Y. Yu, Numerical study of non-uniform cooling heat transfer characteristics of supercritical CO_2 in horizontal air-cooled finned tube, Case Stud. Therm. Eng. 37 (2022) 102263, https://doi.org/10.1016/j.csite.2022.102263.
[19] M. Lata, D.K. Gupta, Simulation and performance evaluation of trans-critical CO_2 refrigeration system with modified evaporative cooled finned tube gas cooler in Indian context, Appl. Therm. Eng. 186 (2021) 116500, https://doi.org/10.1016/j.applthermaleng.2020.116500.
[20] L. Chai, S.A. Tassou, K.M. Tsamos, Simulation and performance evaluation of trans-critical CO_2 refrigeration system integrated with spray-cooled gas coolers, Processes 14 (6) (2026) 903, https://doi.org/10.3390/pr14060903.
[21] G. Petruccelli, T. Turunen-Saaresti, D. Serret, A. Grönman, A. Conrozier, A. M. Dolatabadi, Experimental and numerical investigation of CO_2 condensation in a printed circuit heat exchanger for transcritical power cycles, Appl. Therm. Eng. 278 (2025) 127453, https://doi.org/10.1016/j.applthermaleng.2025.127453.
[22] D.B. Marchetto, M.M. Marinheiro, A.T. de Souza Netto, G. Furlan, G. Ribatski, J. R. Thome, C.B. Tibirica, Condensation flow inside tubes: a review of heat transfer coefficient measurement techniques, experimental databases and prediction methods, Exp. Thermal Fluid Sci. 160 (2025) 111298, https://doi.org/10.1016/j.expthermflusci.2024.111298.
[23] ANSI/ASHRAE Standard 41.2, Standard methods for air velocity and airflow measurement, American Society of Heating Refrigeration and Air-Conditioning Engineers, Inc, Atlanta, USA, GA, 2018.
[24] D. Hellenschmidt, P. Petagna, Effects of saturation temperature on the boiling properties of carbon dioxide in small diameter pipes at low vapour quality: heat transfer coefficient, Int. J. Heat Mass Transf. 172 (2021) 121094, https://doi.org/10.1016/j.ijheatmasstransfer.2021.121094.
[25] M. Kabir, An experimental approach to heat loss measurement of horizontal two-phase flow boiling in low-pressure low-flow (LPLF) conditions, Case Stud. Therm. Eng. 58 (2024) 104419, https://doi.org/10.1016/j.csite.2024.104419.
[26] A.L. London, R.A. Seban, A generalization of the methods of heat exchanger analysis, Int. J. Heat Mass Transf. 23 (1) (1980) 5–16, https://doi.org/10.1016/0017-9310(80)90133-7.
[27] M.M. Shah, Prediction of heat transfer during condensation of carbon dioxide in channels, Appl. Therm. Eng. 93 (2016) 192–199, https://doi.org/10.1016/j.applthermaleng.2015.09.016.
[28] D. Chisholm, A theoretical basis for the Lockhart-Martinelli correlation for two-phase flow, Int. J. Heat Mass Transf. 10 (12) (1967) 1767–1778, https://doi.org/10.1016/0017-9310(67)90047-6.
[29] V. Gnielinski, New equations for heat and mass transfer in turbulent pipe and channel flow, Int. Chem. Eng. 16 (2) (1976) 359–367.
[30] B.S. Petukhov, P.L. Kirillov, About heat transfer at turbulent fluid flow in tubes, Therm. Eng. 4 (1958) 63–68.
[31] C.C. Wang, W.S. Lee, W.J. Sheu, A comparative study of compact enhanced fin-and-tube heat exchangers, Int. J. Heat Mass Transf. 44 (18) (2001) 3565–3573, https://doi.org/10.1016/S0017-9310(01)00011-4.
[32] T.E. Schmidt, Heat transfer calculations for extended surfaces, Refrigerating Engineering 57 (4) (1949) 351–357.
[33] M. Sahami, H. Ghassemi, A. Terziev, G. Pitchurov, Homogeneous condensation in high-speed flows: a review on droplet nucleation and growth models, J. Braz. Soc. Mech. Sci. Eng. 47 (12) (2025) 1–43, https://doi.org/10.1007/s40430-025-05984-1.